

Proton Acceleration by Collisionless Shocks in Supermassive Black Hole Coronae: Implications for High-Energy Neutrinos

MINH NHAT LY  ^{1,2} YOSHIYUKI INOUE, ^{3,4,5} YASUHIKO SENTOKU, ² AND TAKAYOSHI SANO²

¹Department of Physics, Graduate School of Science, The University of Osaka, 1-1 Machikaneyama, Toyonaka, Osaka 560-0043, Japan

²Institute of Laser Engineering, The University of Osaka, 2-6 Yamadaoka, Suita, Osaka 565-0871, Japan.

³Department of Earth and Space Science, Graduate School of Science, The University of Osaka, 1-1 Machikaneyama, Toyonaka, Osaka 560-0043, Japan

⁴Interdisciplinary Theoretical & Mathematical Science Center (iTHEMS), RIKEN, 2-1 Hirosawa, 351-0198, Japan

⁵Kavli Institute for the Physics and Mathematics of the Universe (WPI), UTIAS, The University of Tokyo, 5-1-5 Kashiwanoha, Kashiwa, Chiba 277-8583, Japan

ABSTRACT

Recent observations by the IceCube Neutrino Observatory have revealed a significant excess of high-energy neutrinos from nearby Seyfert galaxies, such as NGC 1068, without a corresponding flux of high-energy gamma-rays. This suggests that neutrinos are produced via hadronic interactions in a region opaque to gamma-rays, likely a hot corona surrounding the central supermassive black hole. However, the mechanism responsible for accelerating the parent protons to the required energies (~ 100 TeV) remains an open question. In this study, we investigate diffusive shock acceleration (DSA) in active galactic nucleus (AGN) coronae using a suite of one-dimensional Particle-in-cell (PIC) simulations spanning a broad range of plasma parameters. We find that DSA is a robust and efficient mechanism for proton acceleration, consistently channeling approximately 10% of the shock's kinetic energy into non-thermal ions, even for shocks with sonic Mach number as low as $M_s \approx 2$. In contrast, the efficiency of electron acceleration is highly variable and less efficient (< 1%) in our parameter survey. These findings provide strong, first-principles support for the hadronic models of neutrino production in AGN and offer quantitative constraints that can explain the observed gamma-ray deficit.

Keywords: High energy astrophysics (739); Shocks (2086); Plasma astrophysics (1261); Active galactic nuclei (16); Particle astrophysics (96); Non-thermal radiation sources (1119)

1. INTRODUCTION

High-energy astrophysical neutrinos are produced in hadronuclear (pp) or photopion ($p\gamma$) interactions of high-energy cosmic rays (CRs). These neutrinos are usually accompanied by a comparable gamma-ray flux according to standard hadronic scenarios, pp and $p\gamma$ (e.g., S. R. Kelner et al. 2006; S. R. Kelner & F. A. Aharonian 2008). Recently, the IceCube Collaboration reported TeV neutrinos from nearby, radio-quiet (RQ) active galactic nuclei (AGNs), most clearly the Seyfert galaxy NGC 1068 (R. Abbasi et al. 2022, 2025). However, the observed gamma-ray fluxes are lower than expected compared to the neutrino fluxes, which cannot be explained by a simple hadronic picture. This discrepancy points to a gamma-ray opaque production site for the neutrinos, although other possibilities are still being discussed (K. Yasuda et al. 2025).

A natural candidate is a hot corona surrounding the central supermassive black hole (SMBH; Y. Inoue et al. 2019; K. Murase et al. 2020). A black hole (BH) corona is a compact, hot plasma with electron temperature $T_e \approx 10^9$ K and a characteristic size of about $100 R_g$, where R_g is the gravitational radius. Protons would be decoupled from electrons and have temperature $T_i \gg T_e$ due to the collisionless nature of the environment (e.g., R. Kawabata & S. Mineshige 2010). In such a region, Comptonized X-ray photons can efficiently attenuate GeV to TeV gamma rays through $\gamma\gamma$ pair production, while neutrinos can escape. In order to explain the IceCube signal, the corona must host parent CRs

accelerated to at least ~ 100 TeV so that secondary pions can produce the observed neutrinos while the associated gamma rays are suppressed (R. Abbasi et al. 2022).

However, the dominant particle acceleration mechanism in SMBH coronae is not yet established. Proposed scenarios include diffusive shock acceleration (DSA; Y. Inoue et al. 2019; Y. Inoue et al. 2020; S. Inoue et al. 2022), stochastic acceleration (SA; K. Murase et al. 2020; A. Kheirandish et al. 2021; R. Mbarek et al. 2024; D. F. G. Fiorillo et al. 2024a), magnetic reconnection (D. F. G. Fiorillo et al. 2024b; D. Karavola et al. 2025), and hybrid cases where these processes act together (e.g., M. Lemoine & F. Rieger 2025, who invoked SA combined with reacceleration in the jet).

Compared to other mechanisms, recent observational results favor DSA. In particular, millimeter observations of nearby Seyferts point to coronal magnetic field strengths of roughly 10 to 100 G (Y. Inoue & A. Doi 2018; Y. Inoue et al. 2020; T. Michiyama et al. 2023; E. Shabloskaya et al. 2024; T. Michiyama et al. 2024; S. d. Palacio et al. 2025; A. Jana et al. 2025; I. M. Mutie et al. 2025, but see also A. Hankla et al. 2025) corresponding to the Alfvén speed of $v_A/c \sim 10^{-2} - 10^{-3}$. Such weak field conditions are generally unfavorable for efficient SA or magnetic reconnection. Nonetheless, the viability of each mechanism under realistic coronal conditions remains a subject of active debate, partly due to the limited first-principles constraints tailored to SMBH coronae.

The largest uncertainty for DSA lies in its efficiency of particle acceleration within coronal plasmas. The hot coronal environment likely results in low sonic Mach number shocks (M_s of order a few), which are traditionally considered to produce weak shocks and thus unable to accelerate particles efficiently (J.-H. Ha et al. 2018; H. Kang et al. 2019; A. J. van Marle 2020). Moreover, the parameter regime for coronal shocks has yet to be explored consistently for both electron and ion dynamics. In particular, the behavior of non-equilibrium, two-temperature plasmas ($T_i \neq T_e$) and the trans-relativistic shock speeds remains poorly understood.

To resolve uncertainties and provide better constraints to DSA as a leading candidate for proton acceleration, we investigate collisionless shocks by employing first-principle, particle-in-cell (PIC) simulations tuned to BH coronal parameters. We survey quasi-parallel shocks across the ranges of sonic Mach number, Alfvénic Mach number, shock velocity and ion-to-electron temperature ratio motivated by observational constraints for Seyferts (Y. Inoue et al. 2019).

This paper is organized as follows. In Section 2, we derive the shock conditions expected in BH coronae. The PIC simulation setup is then described in detail in Section 3. In Section 4, we present our main findings, beginning with the shock structure and a unified picture of particle acceleration from a representative simulation (Section 4.1). We then examine the proton acceleration rate (Section 4.2) and the proton and electron acceleration efficiencies across our parameter survey (Section 4.3). In the discussion (Section 5), we explore the implications of our results for neutrino production in BH coronae, focusing on the well known NGC 1068. We also briefly address electron acceleration in Section 5.2. Finally, we summarize our conclusions in Section 6.

2. SHOCK CONDITIONS IN BH CORONAE

Here, the corona of a supermassive black hole of mass M_{BH} is considered as a hot, collisionless plasma region extending to $R_c \lesssim 100 R_g$, where $R_g = GM_{\text{BH}}/c^2$ is the gravitational radius. We consider a scenario in which shocks form within the BH corona (see Figure 1). Such shocks can naturally arise from infalling material associated with the accretion flow or from failed winds (Y. Inoue et al. 2019; Y. Inoue et al. 2020; S. Inoue et al. 2022). Shocks may also be triggered by material falling in from larger radii, for example from broad-line region clouds (A. L. Müller & G. E. Romero 2020; A. L. Müller et al. 2022; P. Sotomayor & G. E. Romero 2022). In this case, the fallback flow is likely much colder than the BH corona, which we will refer to as the cold inflow scenario.

Kinetic studies of shock-accelerated particles in collisionless plasmas have identified shock sonic and Alfvénic Mach number, M_s and M_A , as the most important quantities to determine characteristics of particle acceleration. In this section, we will derive these shock parameters from the conditions in BH coronae. Our goal is to establish a fiducial range for the shock parameters consistent with multi-messenger observations, thereby providing a physical basis for modeling shock-driven proton acceleration and subsequent neutrino production. For this work, we assume the plasma is primarily composed of ion-electron, where the fraction of positrons is negligible. We treat ions as protons, which constitute the majority of baryonic matter.

For our fiducial model, we assume the shock velocity, v_{sh} , is on the order of the free-fall velocity of infalling material, $v_{\text{ff}} = \sqrt{2GM_{\text{BH}}/R_c}$. This yields the following scaling for shock speed:

$$\frac{v_{\text{sh}}}{c} \simeq 0.14 \left(\frac{r_c}{100} \right)^{-1/2}, \quad (1)$$

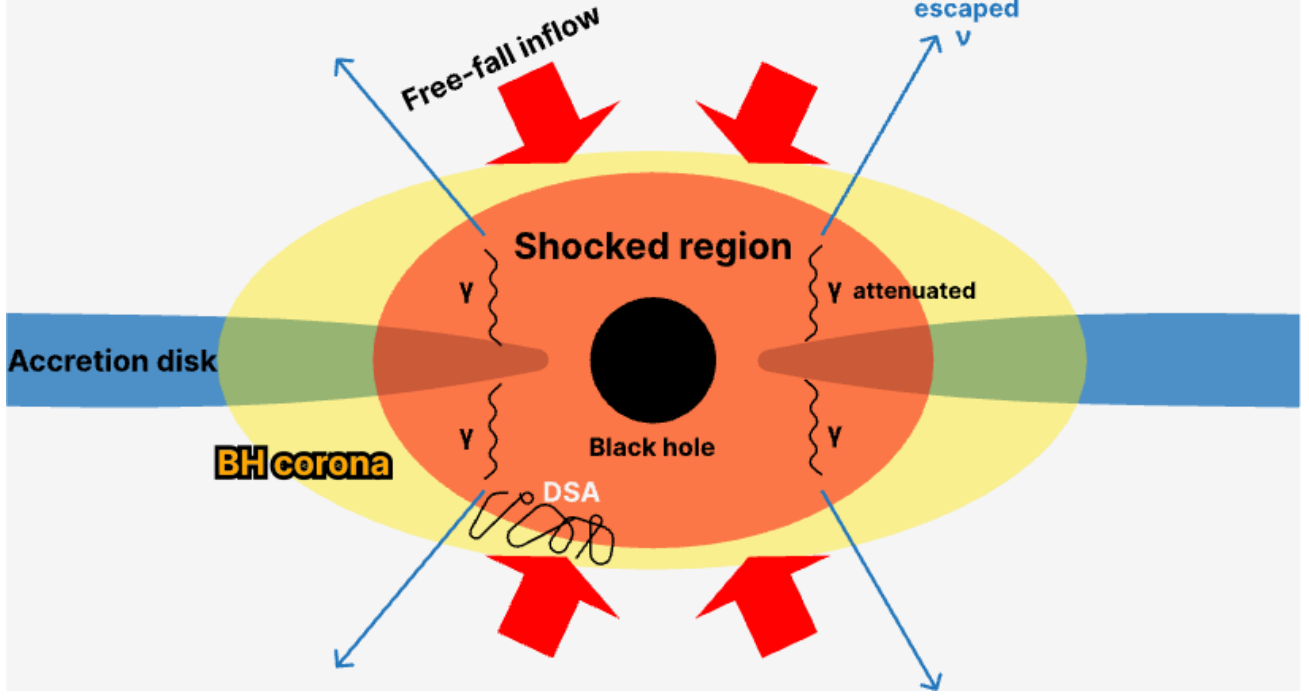


Figure 1. Schematic illustration of an accretion shock formed by the in-falling flow in the hot BH corona. Protons are accelerated to high energies and produce high-energy neutrinos through hadronic pp and $p\gamma$ interactions. Neutrinos can escape from the system and be observed by IceCube, while the accompanying gamma-rays will be attenuated by X-ray photons.

where $r_c = R_c/R_g$ is the coronal radius in the unit of the gravitational radius.

The sonic Mach number $M_s = v_{\text{sh}}/c_s$ depends on the plasma sound speed, $c_s = \sqrt{\gamma_{\text{ad}}(T_i + T_e)/m_i}$, where T_i and T_e denote the ion (proton) and electron temperatures, respectively, and $m_i = m_p$ is the rest mass of the proton. We also adopt an adiabatic index of $\gamma_{\text{ad}} = 5/3$. While the electron temperature can be constrained by the cutoff energy of the X-ray spectrum to $T_e \sim 100$ keV (e.g., A. C. Fabian et al. 2015; S. Laha et al. 2025), the ion temperature is poorly constrained by observations. In BH hot coronae, inefficient Coulomb coupling allows ions to become significantly hotter than electrons ($T_i \gg T_e$). A common assumption of $T_i \sim 10 T_e \sim 1$ MeV leads to

$$M_s = \frac{v_{\text{sh}}}{c_s} \simeq 3.4 \left(\frac{r_c}{100} \right)^{-1/2} \left(\frac{T_i}{1 \text{ MeV}} \right)^{-1/2}. \quad (2)$$

Alternatively, a more physically motivated estimate for T_i comes from advection-dominated accretion flow (ADAF) models, which predict $T_i \simeq GM_{\text{BH}}m_i/(6R_c) \sim 1.6(r_c/100)^{-1}$ MeV (F. Yuan & R. Narayan 2014; Y. Inoue et al. 2024). This temperature profile yields a slight lower Mach number of $M_s \simeq 2.7$ independent of other parameters. From the estimation, shocks in the BH corona are likely to have low sonic Mach numbers. Although higher sonic Mach numbers (up to a few tens) could be realized in the cold inflow picture.

The Alfvénic Mach number, $M_A = v_{\text{sh}}/v_A$, depends on the Alfvén speed, $v_A = B_0/\sqrt{4\pi n_0 m_i}$, which requires estimates for the upstream plasma density n_0 and magnetic field B_0 . We estimate the electron density $n_e = n_0$ from Thompson scattering opacity, $\tau_T = n_e \sigma_T R_c \sim 1$ (Y. Inoue et al. 2019; P. Padovani et al. 2024). The coronal magnetic field B_0 remains a significant source of uncertainty. Millimeter emissions from electron synchrotron radiation are suggested as a method to estimate B_0 , which constrains $B_0 \sim O(10 - 100)$ G (Y. Inoue & A. Doi 2018; S. d. Palacio et al. 2025). For example, the value estimated for NGC1068 is $B_0 \simeq 150$ G (I. M. Mutie et al. 2025; S. d. Palacio et al. 2025). Hence, we adopt $B_0 = 100$ G as the fiducial value for this study. The Alfvén speed and the Alfvénic Mach number are then given by

$$\frac{v_A}{c} \simeq 7.2 \times 10^{-3} \left(\frac{r_c}{100} \right)^{1/2} \left(\frac{M_{\text{BH}}/M_{\odot}}{10^7} \right)^{1/2} \left(\frac{B_0}{100 \text{ G}} \right), \quad (3)$$

$$M_A = \frac{v_{\text{sh}}}{v_A} \simeq 20 \left(\frac{r_c}{100} \right)^{-1} \left(\frac{M_{\text{BH}}/M_{\odot}}{10^7} \right)^{-1/2} \left(\frac{B_0}{100 \text{ G}} \right)^{-1}. \quad (4)$$

It is worth noticing that the estimate of magnetic field strength is still under debate. Other acceleration models, such as SA or reconnection models, require stronger fields ($B \gg 10^3$ G, see e.g., [K. Murase 2022](#); [A. Das et al. 2024](#); [D. F. G. Fiorillo et al. 2024b](#)).

In summary, our theoretical estimates suggest that shocks in the coronae of RQ AGNs are likely to be trans-relativistic ($v_{\text{sh}}/c \sim 0.3$), low sonic Mach numbers ($M_s \sim 2 - 10$), and moderate Alfvén Mach numbers ($M_A \sim 30$). These values are subject to considerable uncertainty, hence, we aim to systematically survey shocks with a wide range of parameters (see details in Table 1). We will focus on the effects that less known from previous collisionless shock studies, like the trans-relativistic shock regime ($v_{\text{sh}}/c \sim 0.3$) and initial ion-to-electron temperature imbalance (T_i/T_e).

3. PIC SIMULATION SETUP

Table 1. Simulation Parameter Survey

Run ID	v_{sh}/c	M_s	M_A	T_i/T_e	$T_e/(m_i c^2)$	$T_i/(m_i c^2)$	Purpose
T10 (Ref)	0.33	8	26	10	9.281×10^{-5}	9.281×10^{-4}	Reference Case
T1	0.33	8	26	1	5.105×10^{-4}	5.105×10^{-4}	
T50	0.33	8	26	50	2.002×10^{-5}	1.001×10^{-3}	Different temperature ratios (T_i/T_e)
T0.01	0.33	8	26	0.01	1.011×10^{-3}	1.011×10^{-5}	
S4T1	0.33	4	26	1	2.042×10^{-3}	2.042×10^{-3}	
S4T10	0.33	4	26	10	3.713×10^{-4}	3.713×10^{-3}	Different temperature ratios with $M_s = 4$
S4T50	0.33	4	26	50	8.007×10^{-5}	4.004×10^{-3}	
S2T1	0.33	2	26	1	8.168×10^{-3}	8.168×10^{-3}	
S2T10	0.33	2	26	10	1.485×10^{-3}	1.485×10^{-2}	Different temperature ratios with $M_s = 2$
S20T1	0.33	20	26	1	8.168×10^{-5}	8.168×10^{-5}	Higher M_s with $T_i = T_e$
S30T0.01	0.33	30	26	0.01	7.188×10^{-5}	7.188×10^{-7}	Higher M_s with hotter electrons
A4	0.33	8	4	10	9.281×10^{-5}	9.281×10^{-4}	
A8	0.33	8	8	10	9.281×10^{-5}	9.281×10^{-4}	Different Alfvén Mach numbers (M_A)
A46	0.33	8	46	10	9.281×10^{-5}	9.281×10^{-4}	
V0.125	0.167	8	26	10	2.377×10^{-5}	2.377×10^{-4}	
V0.5	0.66	8	26	10	3.713×10^{-4}	3.713×10^{-3}	Different shock velocities (v_{sh})

To reveal first-principle and self-consistent description of particle acceleration under the physical conditions of BH coronae, we employ Particle-in-cell (PIC) method. A series of large-scale 1D3V (one spatial dimension, three velocity dimensions) PIC simulations using the code SMILEI ([J. Derouillat et al. 2018](#)) is adopted to survey the parameter space of the shocks in BH coronae.

Suppose a uniform plasma with the density $n_i = n_e$ occupies the region $x > 0$. The plasma is initialized with a velocity $-v_{\text{pt}}$ drifting toward a reflective boundary at $x = 0$ where the incoming and reflected plasma interact and launch a shock toward the $+x$ direction. Shocks modeled this way coincide with the shocks' downstream rest frame, similar to previous studies ([J. Park et al. 2015](#); [M. Shalaby 2024](#)). We introduce the shock compression ratio \mathcal{R} . In the upstream rest frame, the shock velocity is given by $v_{\text{sh}} = v_{\text{pt}} \mathcal{R}/(\mathcal{R} - 1)$. For a strong shock with $\mathcal{R} \approx 4$, this expression reduces to $v_{\text{sh}} \simeq 4v_{\text{pt}}/3$. The magnetic field is initialized in $x - y$ plane = $B_x \hat{x} + B_y \hat{y}$, where $B_x = B_0 \cos \theta$, $B_y = B_0 \sin \theta$, and B_0 denotes the field strength. In this study, we focus on quasi-parallel shocks with a fixed magnetic obliquity $\theta = 30^\circ$.

Simulation parameters are summarized in Table 1. Electrons and protons are initialized with the relativistic Maxwell-Jüttner distribution of T_e and T_i , respectively. We use a reduced ion-to-electron mass ratio of $m_R = m_i/m_e = 100$ to make the simulations computationally feasible but large enough for standard scale-separation between ions and

electrons. Accordingly, the physical parameters (T_i, T_e, B_0) are scaled to preserve the key dimensionless parameters $(M_s, M_A, T_i/T_e)$ and retain the characteristic of shock plasma physics. Note that even if the Mach number is the same, T_i and T_e can vary significantly depending on the temperature ratio T_i/T_e (see Table 1).

We resolved most of simulations with spatial resolution $\Delta x = 0.1 d_e$ and temporal resolution $\Delta t = 0.04 \omega_{pe}^{-1}$, where $\omega_{pe} = \sqrt{4\pi n_0 e^2/m_e}$ and $d_e = c/\omega_{pe}$ are in turn the upstream plasma frequency and electron's inertial length. The only exception is the run A4, where we adopted $\Delta x = 0.025 d_e$ and $\Delta t = 0.02 \omega_{pe}^{-1}$ to resolve the electron Larmor radius $\rho_e = m_e v_{pt} c / (e B_0) \simeq 0.3 d_e$ with proper resolution and ensure the energy conservation. In the simulations, we use 150 particles per cell per species. We find that it is more convenient for the analysis of shock structure and ion acceleration to express time in units of the ion gyrofrequency, $\Omega_{ci} = e B_0 / (m_i c)$ (Sections 4.1 and 4.2). We therefore convert all times to this normalization, using

$$\Omega_{ci} = \omega_{pe} \frac{v_{sh}/c}{M_A \sqrt{m_R}}. \quad (5)$$

All simulations are evolved for at least $t_{\text{end}} \gtrsim 400 \Omega_{ci}^{-1}$, ensuring that the relevant electromagnetic instabilities reach saturation and that a well-developed non-thermal power-law tail emerges in the particle distribution. We use a sufficiently large simulation box size L_x so that reflected particles and those undergoing acceleration remain within the receding plasma for the entire duration up to t_{end} . The length size $L_x = 180224 d_e$ for our typical case and the largest case (run V0.5) reaching $L_x = 294912 d_e$.

4. RESULTS

4.1. Quasi-parallel shock structures

First, let us examine the results of our reference simulation (run T10), in which the plasma parameters are chosen as $M_s = 8$, $M_A = 26$, $v_{pt}/c = 0.25$, and $T_i/T_e = 10$.

4.1.1. Shock structure

Figure 2 displays a snapshot from the reference simulation (run T10) in a quasi-steady evolution stage at $t \approx 256 \Omega_{ci}^{-1}$ ($t = 2 \times 10^5 \omega_{pe}^{-1}$). The shock front is located at $x_{sh} \approx 16000 d_e$ [vertical red dash line in Figure 2(c)], marking the boundary between the upstream (unshocked) and downstream (shocked) regions. The ion density shows a strong compression across the shock, reaching more than four times the upstream density on average ($\mathcal{R} \gtrsim 4$), which signals the formation of a strong shock based on the Rankine-Hugoniot jump conditions. We define x_{sh} throughout this study as the position of the sharp ion density ramp, where $x \leq x_{sh}$ refers as the shock's downstream and $x \geq x_{sh}$ to the upstream region.

In Figures 2(a) and (b), we show the $x - p_x$ phase space distribution of ions and electrons, respectively. The ion phase space [Figures 2(a)] provides direct evidence for ion acceleration, showing an energetic back-streaming population of ions comprising a shock-reflected and accelerated population, both moving away from the shock into the upstream region. This streaming ion population excites magnetic fluctuation modes in the upstream [see Figure 2(e)], providing the necessary scattering environment for electrons and ions to complete multiple shock-crossing cycles characteristic of the DSA process. In addition, the backstreaming ions also generate a net current, which induces a compensating return current in the background electrons. As shown in the electron phase space [Figure 2(b)], this interaction leads to significant electron preheating in the upstream region near the shock front ($x_{sh} < x \lesssim 2.5 \times 10^4 d_e$). This preheating process has recently been shown to play a crucial role in subsequent electron acceleration in quasi-parallel collisionless shocks (S. Gupta et al. 2024a, 2025).

The transverse magnetic field components, B_y and B_z , are shown in Figure 2(d), while their combined magnitude, $B_{\perp} = \sqrt{B_y^2 + B_z^2}$, is presented in Figure 2(e). The transverse magnetic amplitude, B_{\perp} , is amplified by approximately a factor ~ 2 relative to its initial upstream value. As discussed above, this amplification and the associated fluctuations originate from the interaction between the back-streaming ions and the upstream plasma, the detailed mechanism of which will be investigated in the later section.

4.1.2. Particle spectrum and acceleration trajectory

To illustrate how the energy is partitioned between species, each spectrum is plotted as $(\gamma - 1)f(\gamma)$ against the kinetic energy $K = (\gamma - 1)\mu$, where $\mu = m_{i,e}/m_i$ denotes the normalized particle mass. The upper panel (a) of

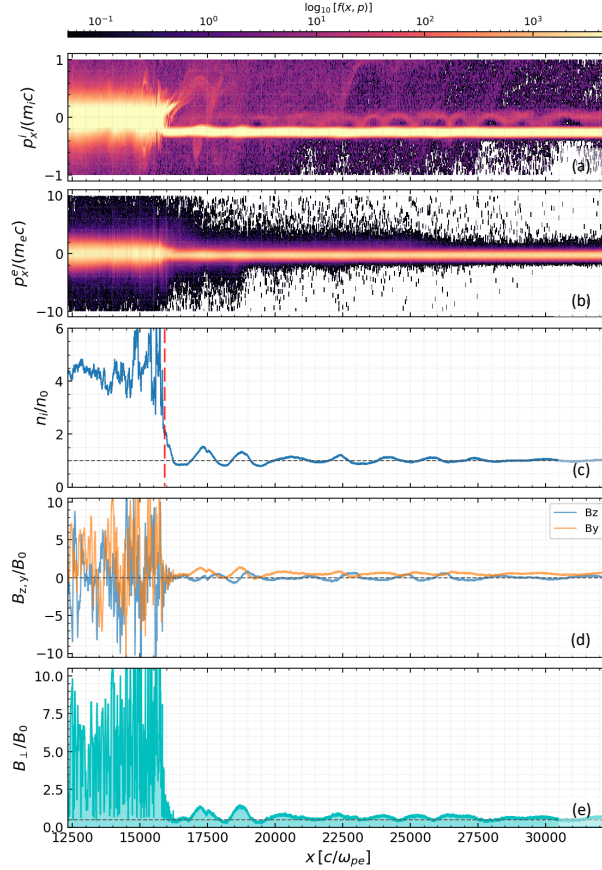


Figure 2. Snapshot of shock structures in fiducial model (run T10) at $t \approx 256 \Omega_{ci}^{-1}$. (a, b) The position-momentum ($x - p_x$) phase space distributions for ions and electrons. (c) Ion density profile, with the shock position (x_{sh}) marked by the red dashed line. (d, e) The transverse magnetic field components (B_y, B_z) and the total transverse amplitude (B_\perp), showing significant amplification over the initial value [black dashed line in (e)].

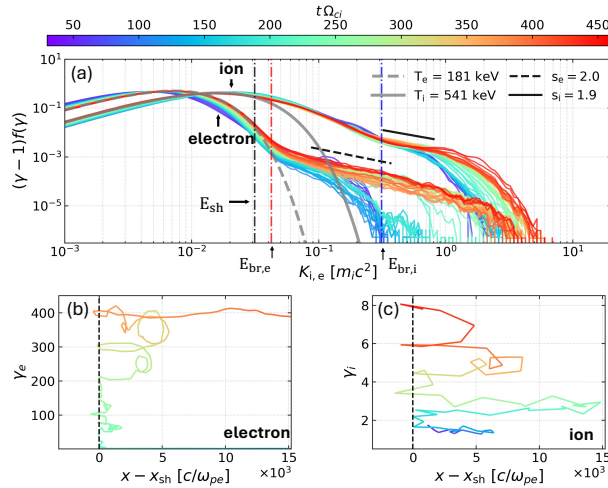


Figure 3. Signatures of particle acceleration, with the color scale indicating time in units of $t\Omega_{ci}$. (a) Evolution of the ion and electron energy spectra in the shock downstream. Both species exhibit two distinct components: a thermal bulk and a developing non-thermal power-law tail. (b, c) Trajectories of a typical accelerating electron and ion, illustrating the DSA process.

Figure 3 shows the temporal evolution of the ion and electron energy spectra in the downstream region of the shock, spanning $x_{\text{sh}} - 6500 d_e < x < x_{\text{sh}} - 1500 d_e$. Unless stated otherwise, this spatial range is adopted for all analyses of the downstream particle spectra. The color gradient represents the simulation time in units of $t\Omega_{\text{ci}}$ shared across all panels in Figure 3.

Both species exhibit clear power-law tails extending from their thermal populations, which can be fitted using a relativistic Maxwellian distribution,

$$f_{\text{MB}}(\gamma) = \frac{\gamma\sqrt{\gamma^2 - 1}}{\Theta K_2(1/\Theta)} \exp\left(-\frac{\gamma}{\Theta}\right), \quad (6)$$

where $\Theta = T/(mc^2)$ is the dimensionless temperature and K_2 is the modified Bessel function of the second kind. The peak of the ion spectrum coincides with the kinetic energy of the incoming flow, $E_{\text{sh}} = \frac{1}{2}m_i v_{\text{pt}}^2$ [vertical black dash-dotted line in Figure 3(a)], indicating that the bulk of the injected energy is deposited into the thermal ions.

The break Lorentz factors γ_{br} , marking the separation point between thermal and non-thermal populations, are shown by red and blue dash-dotted lines for electrons and ions, respectively. While the electron spectra are well fitted by the Maxwellian distribution, the ion spectra exhibit a noticeable supra-thermal shoulder that resembles a shifted Maxwellian, likely arising from pre-acceleration processes at the shock front (D. Caprioli & A. Spitkovsky 2014a; J. Park et al. 2012). Accordingly, based on the transition in particle spectra, we will universally use $\gamma_{\text{br},e} = 10 T_e^{\text{d}}/(m_i c^2)$ and $\gamma_{\text{br},i} = 10 E_{\text{sh}}/(m_i c^2)$ for all cases with T_e^{d} denotes electron downstream temperature. The non-thermal tails follow a power-law distribution, $f(K) \propto K^{-s}$, with the spectral indices $s_i \approx s_e \simeq 2$, consistent with the predictions from DSA theory for strong shocks. In general, ion spectra produced by DSA are hard, with $s_i \lesssim 2$ in most cases and reaching values as low as ~ 1.5 . A power-law index $s = 1.5$ is expected in the non-relativistic energy regime and gradually steepens toward $s_e \sim 2$ in the relativistic limit (C. C. Haggerty & D. Caprioli 2019). In contrast, the electron spectral index varies significantly alter with shock parameters, becoming noticeably softer ($s \gtrsim 3$) for weaker shocks with $M_s \lesssim 8$ (e.g., runs S4T1, S4T10, and S4T50). Further details of the spectral properties across different simulations are summarized in Appendix A.

To illustrate the acceleration mechanism, we tracked a representative electron and ion trajectories in the $x-\gamma$ space, as shown in panels (b) and (c) of Figure 3. Here, we normalized the particle positions relative to the shock front, whereas γ is computed in the simulation frame. The color of each trajectory corresponds to the simulation time and shares the same scale as the upper panel. The ion trajectory shows that the particle resides predominantly in the upstream region and undergoes repeated scattering between the upstream and downstream regions. The ion Lorentz factor γ increases each time the particle returns to the shock front after scattering off upstream fluctuations. This apparent “energy gain” occurs in the downstream frame; if transformed to the shock frame, the particle gains energy upon each shock crossing, as commonly described in DSA theory (see Figure 8 of T. N. Kato 2015).

The electron’s acceleration reveals a more complex, two-stage process. The accelerated electron first undergoes a rapid pre-acceleration phase close to the shock front, with its trajectory resembles a hybrid shock drift acceleration (SDA), a process similar to that described in previous work (J. Park et al. 2015). Once it attains sufficient energy from this initial stage, it is injected into the main DSA cycle for further energization in a similar manner as ions. The significant mass difference between electrons and ions directly impacts their acceleration efficiency. Due to their much smaller gyroradii, electrons require more DSA cycles to achieve the same energy as ions. This lower efficiency results in a smaller non-thermal energy fraction for electrons compared to ions as we can see from the energy spectra shown in Figure 3(a).

4.1.3. Streaming instabilities

The nature of the instabilities driven by streaming ions depends primarily on the ion current density (A. Marcowith et al. 2021; C. C. Haggerty & D. Caprioli 2019). In weak current regimes, the system is dominated by the resonant instability (RI), which is excited through a gyroresonant interaction between the streaming ions and Alfvénic fluctuation (J. Skilling 1971). In contrast, at sufficiently high current densities, a strong neutralizing return current is carried by background electrons, and it excites modes at shorter wavelengths, leading to the non-resonant instability (NRI), so-called Bell’s instability (A. R. Bell 2004). Kinetic plasma studies provide a practical method for distinguishing between them based on the wave polarization: the fastest growing NRI modes are predominantly right-handed (RH), whereas for RI, the left-handed (LH) component is expected to be of greater magnitude (C. C. Haggerty & D. Caprioli 2019; S. Gupta et al. 2024b).

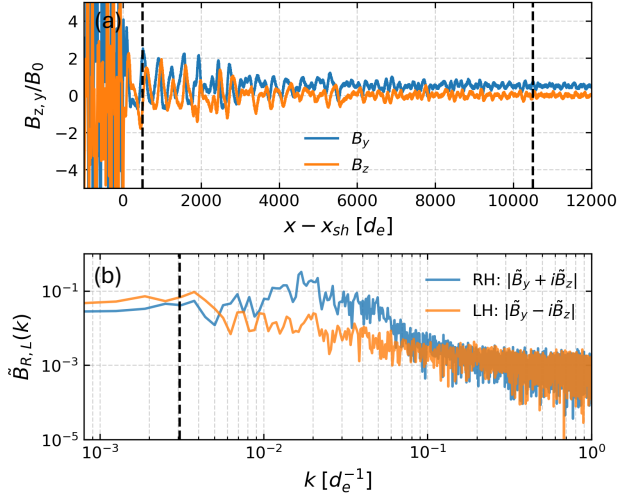


Figure 4. Spatial Fourier analysis of the upstream streaming instability at $t \approx 130 \Omega_{\text{ci}}^{-1}$, showing that the dominant mode is the right-hand non-resonant instability. (a) Transverse magnetic field profile in the upstream region selected for the spectral analysis, indicated by the two vertical black dashed lines. (b) Fourier power spectrum of the magnetic field, decomposed into right-hand (RH) and left-hand (LH) polarized modes. The vertical black dashed line marks the wavenumber of the mode resonant with back-streaming ions of mean gyroradius $\bar{\rho}_i$, $k_{\text{res}} \sim 1/\bar{\rho}_i$.

To study the source of the upstream magnetic turbulence in run T10, we performed a spatial Fourier analysis of the transverse magnetic field in the upstream region at $t \approx 130 \Omega_{\text{ci}}^{-1}$, as indicated by the two vertical black dashed lines in Figure 4(a). The corresponding magnetic amplitude spectra of the RH and LH polarized modes, defined respectively as $\tilde{B}_R = |\tilde{B}_y(k) + i\tilde{B}_z(k)|$ and $\tilde{B}_L = |\tilde{B}_y(k) - i\tilde{B}_z(k)|$, are shown in panel (b). Here \tilde{B}_y, z is the spatial Fourier amplitude in the transverse directions. The RH mode clearly dominates over the LH mode, exhibiting a significantly larger peak amplitude. The spectrum peaks at a wavenumber k_{max} larger than wavenumber of the mode resonant with back-streaming ions $k_{\text{res}} \sim 1/\bar{\rho}_i$ indicated by vertical black dashed line in Figure 4(b). Here, $\bar{\rho}_i$ is the mean gyroradius of the back-streaming ions which can be estimated using $v \approx 5v_{\text{sh}}/4$ corresponding to the velocity of reflected particles in the downstream frame of a strong shock. This behavior is consistent with the expected characteristics of of NRI mode.

We performed a similar analysis for all simulation cases in the present study and found that almost all cases exhibit the NRI as the dominant mode. A few exceptions occur in the low-Alfvénic-Mach-number runs with $M_A = 4$ and 8 (runs A4 and A8). This trend is consistent with previous numerical studies of quasi-parallel collisionless shocks, which report that low- M_A shocks preferentially excite the RI (D. Caprioli & A. Spitkovsky 2014b; S. Gupta et al. 2024b). Nevertheless, both types of instabilities are capable of generating sufficient upstream magnetic turbulence to sustain DSA of both ions and electrons.

4.2. Proton acceleration

We now extend our analysis to quantify the dependence of the proton energy gain or acceleration rate on various shock parameters. In particular, we discuss how the acceleration timescale evolves and what implications it has for potential neutrino emission from the corona.

4.2.1. Dependence on T_i/T_e and M_s

To illustrate how the maximum ion energy evolves over time, Figure 5 shows the time evolution of the average Lorentz factor $\gamma(t)$ of the ten most energetic protons at each snapshot in each simulation. All cases in Figure 5 share the same initial drift velocity ($v_{\text{pt}}/c = 0.25$) and magnetic field strength ($M_A = 26$). The top panels display the simulations with different T_i/T_e values at fixed Mach numbers: $M_s = 8$ in panel (a) and $M_s = 4$ in panel (b). In contrast, the bottom panels compare cases with different M_s values while keeping T_i/T_e constant: $T_i/T_e = 1$ in panel (c), and $T_i/T_e = 10$ (blue lines) and $T_i/T_e = 0.01$ (red lines) in panel (d).

In all cases, the ion energy $\gamma(t)$ evolves in two distinct phases, separated around $t \sim 100 \Omega_{\text{ci}}^{-1}$. The early phase corresponds to the period required for the shock structure to reach a quasi-steady state and for upstream turbulence to fully develop. In the later stage ($t \gtrsim 100 \Omega_{\text{ci}}^{-1}$), the energy gain proceeds approximately linearly with time, $\gamma(t) \propto t$,

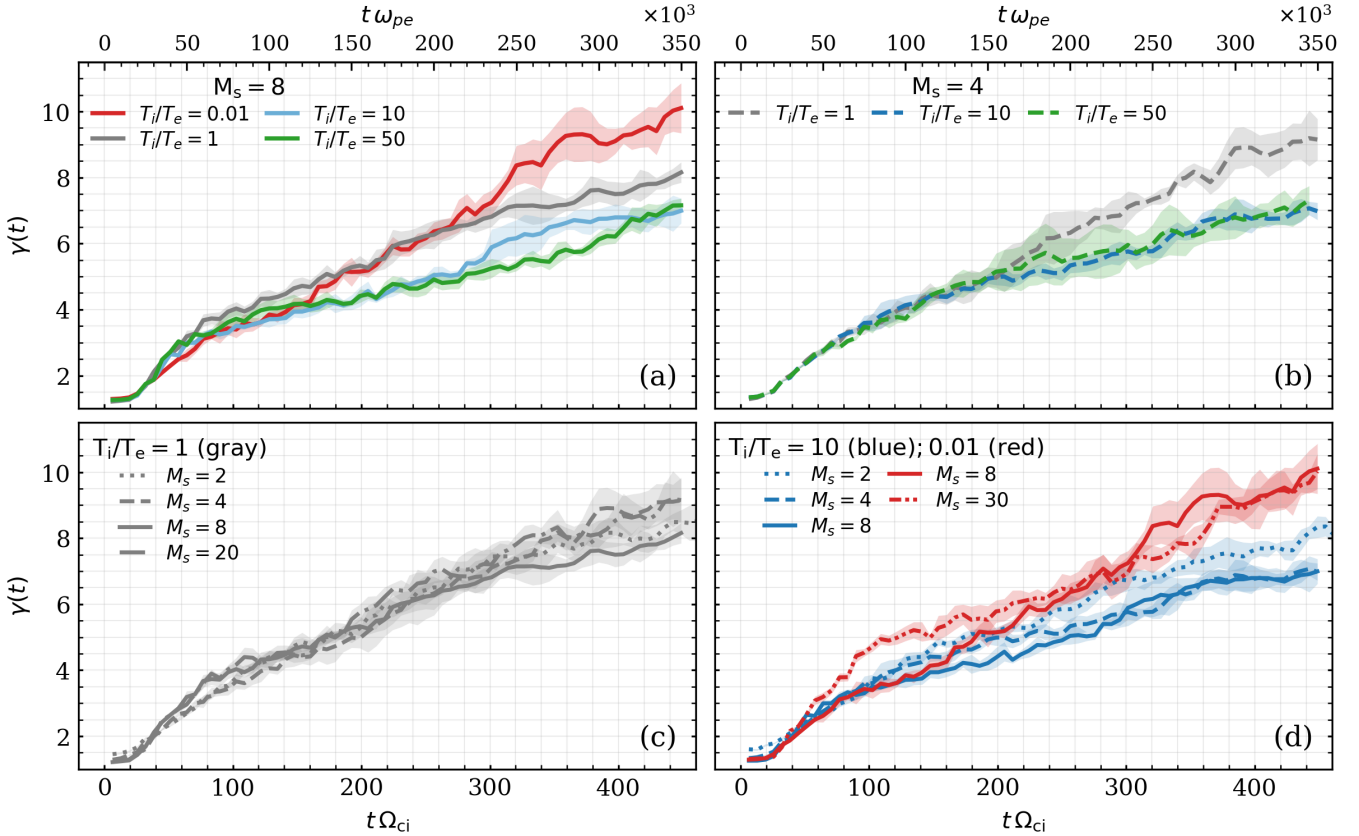


Figure 5. Time evolution of the mean Lorentz factor $\gamma(t)$ of the ten most energetic ions at each snapshot for different plasma conditions. The upper panels show the effect of varying the temperature ratio T_i/T_e at fixed M_s , while the lower panels show the effect of varying M_s at fixed T_i/T_e . Shaded regions represent one standard deviation. All other parameters are identical to the reference run (T10), unless otherwise noted. (a–b) Dependence on T_i/T_e for $M_s = 8$ and $M_s = 4$, respectively. (c) Dependence on M_s for $T_i/T_e = 1$. (d) Same as (c), but for both $T_i/T_e = 0.01$ (red lines) and $T_i/T_e = 10$ (blue lines).

consistent with the prediction of DSA theory (e.g. L. O. Drury 1983; R. Blandford & D. Eichler 1987). Figures 5(a) and (b) show that increasing the temperature ratio T_i/T_e leads to a weak inverse correlation with the acceleration rate, roughly following $\gamma(t) \propto (T_i/T_e)^{-0.15}$. However, this dependence is weak even between the extreme cases of $T_i/T_e = 0.01$ and $T_i/T_e = 50$. At the end of the runs $\gamma(t)$ differs by a factor $\lesssim 1.5$. The sonic Mach number M_s also appears to have no effect on the maximum ion energy, as shown in Figures 5(c) and (d), where cases with the same T_i/T_e (lines of the same color) converge to nearly identical values.

4.2.2. Dependence on M_A and v_{pt}

We next examine the influence of the Alfvénic Mach number M_A and the injected particle velocity v_{pt} . According to DSA theory, the acceleration timescale depends on the magnetic field strength and the shock velocity as $t(\gamma) \simeq D(\gamma)/v_{\text{sh}}^2$, where the diffusion coefficient is approximately Bohm-like, $D(\gamma) \simeq cE_{\text{CR}}/(eB)$ where $E_{\text{CR}} \simeq \gamma m_i c^2$ (L. O. Drury 1983; R. Blandford & D. Eichler 1987). This yields the scaling

$$t(\gamma) \approx \mathcal{C} \gamma \beta_{\text{sh}}^{-2} \Omega_{\text{ci}}^{-1}, \quad (7)$$

where $\beta_{\text{sh}} = v_{\text{sh}}/c$ and \mathcal{C} represents a dimensionless coefficient that encapsulates other factors governing the acceleration efficiency, such as the gyrofactor η_g and acceleration efficiency η_{acc} . Hence, we express time in units of Ω_{ci}^{-1} . When comparing cases with different shock velocities, we normalize the acceleration rate by $(\gamma - \gamma_{\text{sh}})\beta_{\text{sh}}^{-2}$ in order to factor out the expected DSA scaling [Figure 6(b)].

Figures 6(a) and (b) illustrate the effects of varying M_A and v_{pt}/c , respectively. As shown in Figure 6(a), cases with different Alfvénic Mach numbers exhibit broadly similar behaviors, except for the very low $M_A = 4$ case, which

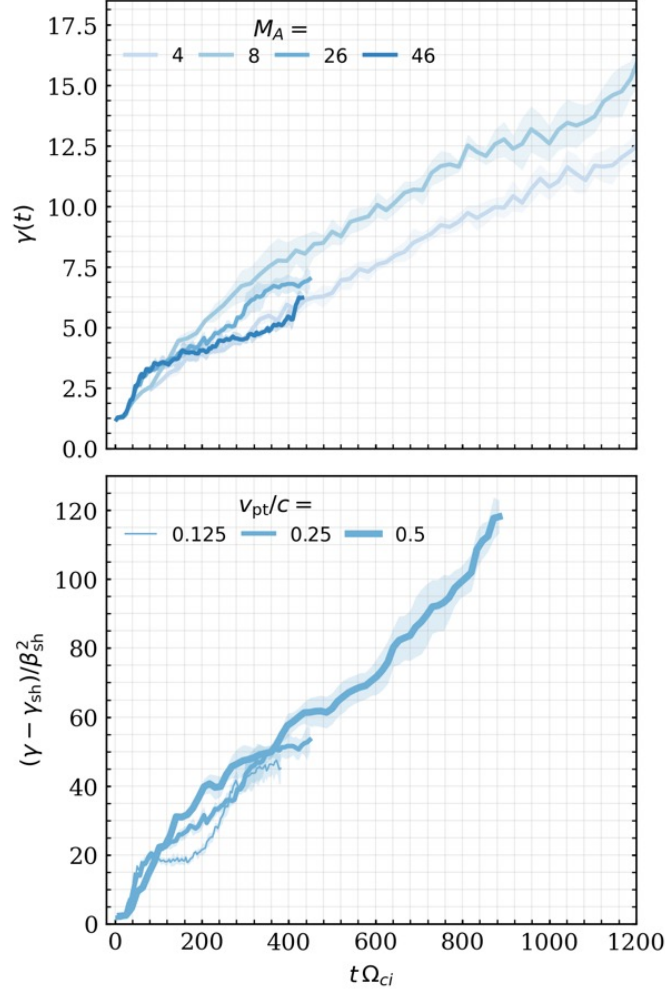


Figure 6. Same format as Figure 5, but showing the dependence on the Alfvénic Mach number and the injected particle velocity. (a) Time evolution of the mean Lorentz factor of the ten most energetic ions for different M_A . (b) Normalized energy gain, $(\gamma - \gamma_{\text{sh}})\beta_{\text{sh}}^2$, for different injected velocities v_{pt}/c . Shaded regions indicate one standard deviation. All other parameters are identical to the reference run (T10), unless otherwise specified.

shows a slightly reduced acceleration rate compared to the reference run ($M_A = 26$). This is likely due to weaker self-generated turbulence, as confirmed by the presence of resonant streaming instability (S. Gupta et al. 2024b). Such a trend is expected, as the shock's Alfvénic Mach number must exceed order unity for efficient particle acceleration to occur (see J. Vink & R. Yamazaki (2014), who predicted a threshold of $M_A \simeq 5/2$). Accordingly, the acceleration rate, \mathcal{C}^{-1} , is expected to decrease significantly as $M_A \rightarrow 1$. When the injection velocity varies from $v_{\text{pt}}/c = 0.125$ to 0.5 in Figure 6(b), the normalized acceleration rates in all three runs remain remarkably similar, confirming that the acceleration efficiency, \mathcal{C} , follows the scaling predicted by Equation (7).

4.2.3. Scaling of acceleration rate

We next compare the normalized acceleration rate, $\mathcal{C}^{-1} = d(\gamma\beta_{\text{sh}}^{-2})/d(t\Omega_{\text{ci}})$, shown in Figure 7. This coefficient is obtained from the slope of the mean energy gain during the late stage of acceleration [$t \gtrsim 100 \Omega_{\text{ci}}^{-1}$; see, e.g., Figure 6(b)]. As clearly seen in Figure 7, the typical value of the normalized acceleration rate is $\mathcal{C}^{-1} \simeq 0.1$, varying by less than a factor of two across all parameter sets.

The reference parameters for Figure 7 are $M_A = 26$, $M_s = 8$, $T_i/T_e = 10$, and $v_{\text{pt}}/c = 0.25$. Each panel varies one parameter while keeping the others fixed: T_i/T_e in (a) (colored lines for different M_s), M_s in (b) (colored lines for different T_i/T_e), v_{pt}/c in (c), and M_A in (d). The results show no clear dependence on M_s [Figure 7(b)] and only a

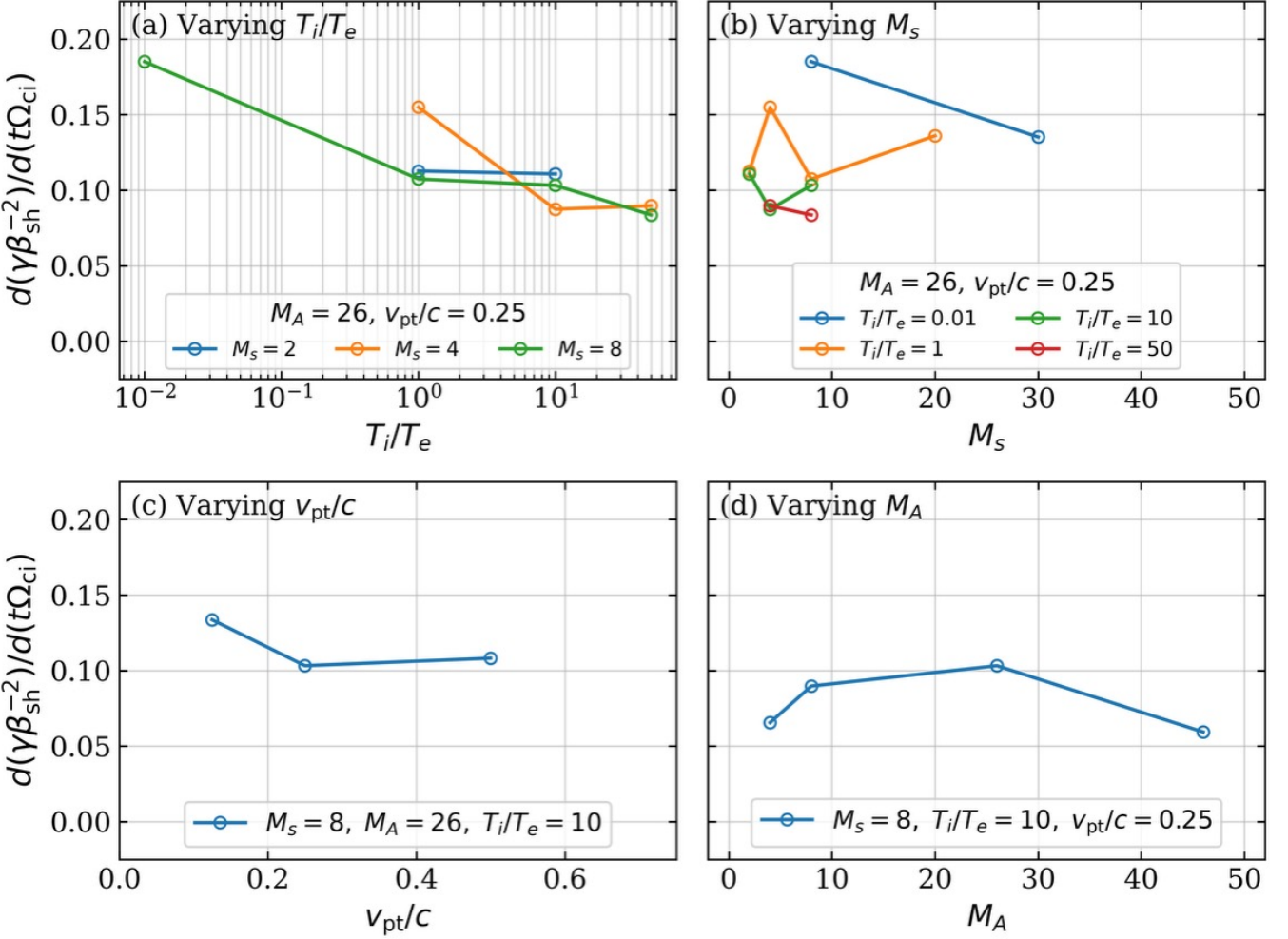


Figure 7. The normalized acceleration coefficient $d(\gamma/\beta_{\text{sh}}^2)/d(t\Omega_{\text{ci}})$ or the slope in Figures 5 and 6, as a function of key shock parameters, calculated from the linear slope of the energy gain at late times. (a) Dependence on T_i/T_e . (b) and (c) Dependence on M_s and M_A , respectively. (d) Dependence on v_{pt}/c .

weak, nearly flat trend with v_{pt}/c [Figure 7(c)]. A slight systematic decrease is observed as ions become hotter relative to electrons (i.e., with increasing T_i/T_e).

Panel (d) indicates a modest dependence of the acceleration rate on the Alfvénic Mach number. While the acceleration efficiency is somewhat reduced at both low and high M_A , it remains comparable over the full range considered. The reduced acceleration efficiency at low M_A likely results from weaker self-generated turbulence, as discussed in Section 4.2.2. This trend is broadly expected from behavior At very high M_A , however, the strong turbulence can excite Short Large-Amplitude Magnetic Structures (SLAMS), which intermittently render parts of the shock superluminal and disrupt ion acceleration (see V. Zeković et al. (2025) for a detailed discussion). This trend suggests the existence of an optimal magnetic field strength for efficient ion acceleration by DSA in this regime.

To summarize, we have demonstrated that ions are efficiently accelerated over a broad range of physical conditions, indicating a robust capability of shocks for ion energization in BH coronae. Remarkably, the normalized acceleration rate varies by less than a factor of two across all tested parameters, consistent with the expectations from DSA theory.

4.3. Energy partition

In this section, we investigate the partitioning of the shock energy into non-thermal ions and electrons (i.e., the acceleration efficiency), which is crucial for determining the relative power available for hadronic neutrino production and leptonic emission.

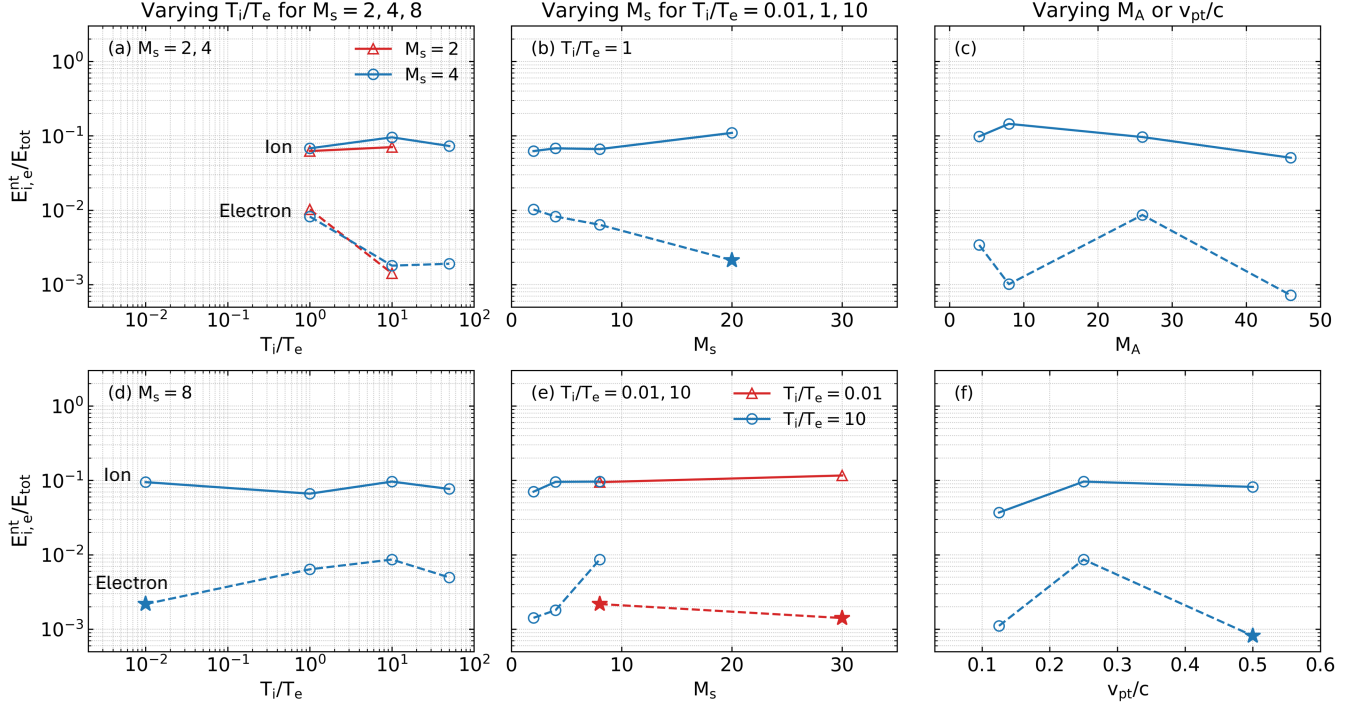


Figure 8. Fraction of non-thermal ion (solid lines) and electron (dashed lines) energy to total energy in the particle spectra across the parameter space. Non-thermal ions are efficiently accelerated, receiving $\sim 10\%$ of the total energy, while electrons remain much less efficient ($< 1\%$) or even suppressed in cases indicated by the \star symbol. Left panels: the effect of T_i/T_e ratio with fixed $M_s = 2$ (red lines) and $M_s = 4$ (blue lines) in panel (a), and $M_s = 4$ in panel (d). Middle panels: the scaling with M_s when T_i/T_e is fixed at $T_i/T_e = 1$ in panel (b), and $T_i/T_e = 0.01$ (red) and $T_i/T_e = 10$ in panel (e). Right panels: variation with (c) M_A and (f) v_{pt}/c . Unless explicitly stated otherwise, other parameters follow $T_i/T_e = 10$, $M_s = 8$, $M_A = 26$, and $v_{\text{pt}}/c = 0.25$.

We define the energy fraction, or the acceleration efficiency, as

$$\frac{E_j^k}{E_{\text{tot}}} = \frac{1}{E_{\text{tot}}} \int d\gamma (\gamma - 1) m_j c^2 f_j^k(\gamma), \quad (8)$$

where $j \in \{i, e\}$ and $k \in \{\text{nt, th}\}$ denotes four different particle energy fractions $E_i^{\text{nt}}, E_e^{\text{nt}}, E_i^{\text{th}}$ or E_e^{th} , corresponding to energy fractions of non-thermal ions, non-thermal electrons, thermal ions, and thermal electrons, respectively. The total particle energy is given by $E_{\text{tot}} = \sum_j^k \int d\gamma (\gamma - 1) m_j c^2 f_j^k(\gamma)$, i.e., the sum of all particle energy. We used the same distinction between thermal and non-thermal populations of ions and electrons as in Section 4.1.2.

The detailed scaling of the energy fractions of non-thermal ions (solid lines) and electrons (dashed lines) is depicted in Figure 8. Each line in the panels then represents a parameter scan, varying one of these values while all others are held constant. Unless otherwise noted, the default parameters are those of the fiducial run T10: $M_A = 26$, $M_s = 8$, $v_{\text{pt}}/c = 0.25$, and $T_i/T_e = 10$. We present results for the scaling with varying T_i/T_e (also with a few M_s values) in the left panels (a) and (d); with varying M_s (with three T_i/T_e values) in the middle panels (b) and (e); and with M_A and v_{pt}/c in panels (c) and (f), respectively.

Remarkably, we find that non-thermal ions are efficiently accelerated, consistently receiving $\sim 10\%$ of the total energy. This high ion acceleration efficiency remains robust across all parameter surveys, even in the low sonic Mach number regime where inefficient acceleration is often assumed. As shown in the left (a, d) and middle (b, e) panels, the ion energy fraction $E_i^{\text{nt}}/E_{\text{tot}}$ remains nearly independent of T_i/T_e and M_s across all tested regimes. Similarly, Figures 8 (c) and (f) show a weak dependence on M_A and v_{pt}/c , with the ion acceleration efficiency slightly reduced at high M_A [panel (c)] and for slower shocks [panel (f)].

The electron acceleration efficiency is much lower than that of ions, with $E_e^{\text{nt}}/E_{\text{tot}}$ remaining below 1%. It also exhibits a more complex dependence, being highly sensitive to the upstream plasma parameters. A major contributing factor is that, in some cases with $v_{\text{pt}}/c \geq 0.25$, we found the maximum energy of the electron power-law tail does not

continue to grow with time, leading to a significant reduction in the acceleration efficiency. We mark such cases with the star symbol in Figure 8, for example, in the $T_i/T_e = 0.01$ runs in panel (e) (red dashed line) and the $v_{\text{pt}}/c = 0.5$ run in panel (f). The physical origin of this behavior is briefly discussed in Section 5.2; however, because electrons remain energetically subdominant, this effect does not affect the ion acceleration results or the overall energy partition discussed above.

Most notably, for implications relevant to BH coronae, $E_e^{\text{nt}}/E_{\text{tot}}$ shows a monotonically decreasing trend with increasing ion-to-electron temperature ratio T_i/T_e , as seen in panels (a) and (d). For $T_i/T_e = 1$, the efficiency is $\sim 10^{-2}$, whereas for high $T_i/T_e \gtrsim 10$, it decreases to $\sim 10^{-3}$. This result agrees with recent work on the electron injection threshold in quasi-parallel shocks (S. Gupta et al. 2025), which indicates that higher electron-thermal speeds in the immediate upstream region favor more efficient electron acceleration. The decline of electron acceleration in high T_i/T_e environments, which is expected in BH coronae, imposes a strong constraint on the multi-messenger emission from these regions. In particular, setting the limits for the energy budget for neutrino production by the hadronic component and the primary leptons' budget for the synchrotron and inverse-Compton emissions.

5. DISCUSSION

In this section, we first synthesize our results on proton acceleration to examine the case of NGC 1068, the most prominent candidate in the IceCube neutrino survey. We then briefly discuss electron acceleration, or rather the lack thereof, in our simulations.

5.1. Implication for neutrino emissions from NGC1068

Here, we explore the implications of our results for neutrino emissions from NGC1068 - the most prominent detection from IceCube observatory up-to-date (R. Abbasi et al. 2022). The detection constrained in the neutrino energy range $E_{\nu} = 1.5 - 15$ TeV, which imply the presence of protons with energy range $E \approx 30 - 300$ TeV. To reach such energies, the proton acceleration timescale must be shorter than the timescales associated with energy losses from cooling and neutrino production. We therefore begin by comparing these relevant timescales. Then, we examine whether the acceleration efficiency of protons inferred from our results (Section 4.3) can fulfill the energy budget for the neutrino spectrum from the object.

In the following analysis, we adopt a set of coronal parameters for NGC 1068 listed in P. Padovani et al. (2024), which we use consistently throughout this discussion unless stated otherwise. We assume a black hole mass of $M_{\text{BH}} = 10^{7.2} M_{\odot}$ and a characteristic coronal size of $R_c = 20 R_g$. The coronal photon field consists of a multi-temperature blackbody emission from the accretion disk (N. I. Shakura & R. A. Sunyaev 1973), parameterized as $L_{\text{disk}} \propto E^{4/3} \exp(-E/E_{\text{cut}})$ with $E_{\text{cut}} = 30$ eV, together with a Comptonized X-ray component described by $L_X \propto E^{1-\Gamma_X} \exp(-E/E_{\text{cut},X})$, where $E_{\text{cut},X} = 128$ keV and $\Gamma_X = 1.95$. Assuming a luminosity distance of $d_L = 10$ Mpc, this corresponds to an integrated disk luminosity of $L_{\text{disk}} = 5 \times 10^{44}$ erg s $^{-1}$ and a 2–10 keV X-ray luminosity of $L_{2-10 \text{ keV}} = 4 \times 10^{43}$ erg s $^{-1}$.

5.1.1. Timescales

In the scenario shown in Figure 1 discussed in Section 2, the dynamical timescale is determined by the free-fall time,

$$t_{\text{fall}} = \frac{R_c}{v_{\text{ff}}} \simeq 0.52 \times 10^4 \left(\frac{r_c}{20} \right)^{3/2} \left(\frac{M_{\text{BH}}/M_{\odot}}{10^{7.2}} \right) [\text{s}] . \quad (9)$$

All the related timescales are summarized in Figure 9 as a function of proton energy.

To account for the observed neutrino emission, protons must be accelerated to energies of $E_p \sim 100$ TeV. At these energies, in addition to hadronic pion production via pp and $p\gamma$ interactions, protons also experience energy losses through the Bethe–Heitler pair production process. We compute the corresponding cooling timescales for Bethe–Heitler (t_{BH}), photomeson ($t_{p\gamma}$), and proton–proton (t_{pp}) interactions using the coronal photon field and parameters defined above. The detailed calculation procedures follow those outlined in Y. Inoue et al. (2019).

For proton acceleration timescale t_{acc} , we make use of our result obtained from Section 4.2. In particular, we adopt the scaling of Equation (7) with the typical value of $\mathcal{C}^{-1} = d(\gamma\beta_{\text{sh}}^{-2})/d(t\Omega_{\text{ci}}) \simeq 0.1$. The scaling for proton acceleration timescale reads

$$\begin{aligned} t_{\text{acc}} &\simeq \mathcal{C}\gamma\beta_{\text{sh}}^{-2}\Omega_{\text{ci}}^{-1} \\ &\simeq 11.1 \left(\frac{E_p}{100 \text{ TeV}} \right) \left(\frac{\mathcal{C}^{-1}}{0.1} \right)^{-1} \left(\frac{\beta_{\text{sh}}}{0.32} \right)^{-2} \left(\frac{B_0}{100 \text{ G}} \right)^{-1} [\text{s}] . \end{aligned} \quad (10)$$

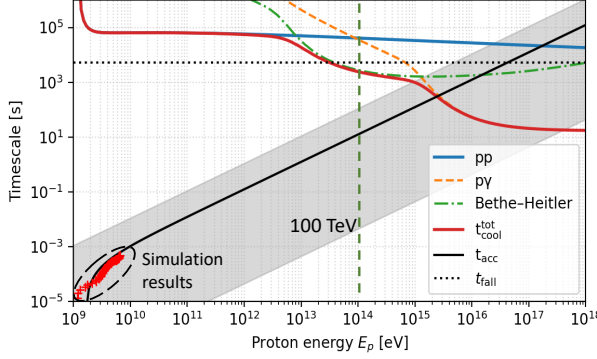


Figure 9. Various timescales in the BH corona of NGC 1068 as a function of proton energy. The typical acceleration timescale t_{acc} (solid black line) is calculated using Equation (10) with $B_0 = 100$ G and $\beta_{\text{sh}} = 0.32$. The free-fall timescale t_{fall} (dotted black line) is calculated using Equation (9). The simulation results taken from run T10 give the normalization of t_{acc} . The gray shade indicates the acceleration timescale range when we varying $B_0 = 10 - 1000$ G and $\beta_{\text{sh}} = 0.1 - 0.5$. The cooling timescales for pp interactions t_{pp} (blue line), $p\gamma$ interactions $t_{p\gamma}$ (orange dashed line), and Bethe-Heitler pair production t_{BH} (green dashed-dotted line) are calculated following the methods in Y. Inoue et al. (2019). The total cooling timescale t_{cool} (red line) is obtained by combining all cooling processes. We include the vertical green dashed line showing proton of 100 TeV energy which required to explain TeV neutrino.

In Figure 9, we extrapolate the simulation scaling given by Equation (10) to several orders of magnitude assuming the continuous evolution.

In addition to the balance between acceleration and cooling timescales, the maximum proton energy is constrained by the finite size of the BH corona region. This geometrical constraint, $\rho_i \lesssim R_c$, is known as the Hillas limit (A. M. Hillas 1984) and implies a maximum achievable energy $E_{\text{max}} \lesssim eB_0R_c$. In the context of DSA, a tighter constraint is often applied, taking the form $E_{\text{max}} \lesssim eB_0R_c\beta_{\text{sh}}$ (L. O. Drury 2012; M. Oka et al. 2025), which yields the following scaling

$$E_{p,\text{max}} \lesssim 467 \left(\frac{B}{100 \text{ G}} \right) \left(\frac{r_c}{20} \right) \left(\frac{M_{\text{BH}}/M_{\odot}}{10^{7.2}} \right) \left(\frac{\beta_{\text{sh}}}{0.32} \right) [\text{PeV}] . \quad (11)$$

Equation (11) shows that the Hillas criterion allows proton acceleration up to energies of ~ 100 TeV, provided that the magnetic field strength satisfies $B_0 \gtrsim 10$ G and the shock velocity fulfills $\beta_{\text{sh}} \gtrsim 10^{-2}$. Moreover, as shown in Figure 9, the acceleration timescale t_{acc} remains shorter than the total cooling timescale t_{cool} up to proton energies of $E_p \sim 1$ PeV for the same range of parameters. Hence, these results demonstrate that our DSA framework can provide a robust mechanism for supplying the high-energy protons responsible for the high-energy neutrinos in the energy range observed by IceCube.

5.1.2. Energy budget

Finally, we discuss whether the acceleration efficiency derived from our simulations ($E_p^{\text{nt}}/E_{\text{tot}} \approx 10\%$) is sufficient to produce the observed neutrino flux. In the scenario of a spherical shock with $R_{\text{sh}} \simeq R_c$ as we assume here, the bound of shock power can be simply estimated as

$$\begin{aligned} L_{\text{sh}} &= \frac{1}{2} n_i m_i v_{\text{sh}}^3 (4\pi R_{\text{sh}}^2) \\ &\simeq 7.3 \times 10^{44} \left(\frac{r_c}{20} \right) \left(\frac{M_{\text{BH}}/M_{\odot}}{10^{7.2}} \right) \left(\frac{v_{\text{sh}}/c}{0.32} \right)^3 [\text{erg/s}] , \end{aligned} \quad (12)$$

where we assume $n_i \simeq n_e \simeq (\sigma_T R_c)^{-1}$.

According to the latest IceCube report (R. Abbasi et al. 2025), the best fit flux at 1 TeV is $\Phi_{\nu} = 4.7_{-1.3}^{+1.1} \times 10^{-11} \text{ TeV}^{-1} \text{ cm}^{-2} \text{ s}^{-1}$ or the neutrino luminosity $L_{\nu} \approx 4\pi d_L^2 E_{\nu}^2 \Phi_{\nu} \simeq 9 \times 10^{41} \times [d_L/(10 \text{ Mpc})]^2 \text{ erg/s}$. The non-thermal proton luminosity required to produce such neutrino luminosity can be estimated as

$$L_p^{\text{nt}} \approx \frac{\mathcal{S} L_{\nu}}{f_{\nu}} , \quad (13)$$

where f_ν is the per flavor production fraction, and $\mathcal{S} \geq 1$ is a spectral-shape factor that accounts for the continuous nature of the non-thermal proton spectrum. Neutrino with $E_\nu = 1$ TeV is produced by protons with the energy $E_p \sim 20E_\nu \sim 20$ TeV which mainly produced neutrinos through pp interactions (Figure 9). Hence, we adopt $f_\nu \sim 1/6$ and $\mathcal{S} \gtrsim 4$ for a proton spectrum with power-law index $s_p = 2$ as seen in most of our simulations. The required non-thermal proton luminosity is therefore $L_p^{\text{nt}} \approx 2.2 \times 10^{43} \text{ erg s}^{-1}$, corresponding to a fractional power $L_p^{\text{nt}}/L_{\text{sh}} \approx 0.03$, well below the proton acceleration efficiency inferred from our simulations (e.g. $E_p^{\text{nt}}/E_{\text{sh}} \sim 0.1$). Consequently, the collisionless shock can readily supply sufficient power to account for the neutrino luminosity observed from NGC 1068.

Finally, we want to stress that this estimation aims to put our results into perspective and provide an intuitive picture of neutrino production in NGC 1068. We acknowledge that applying results from local, first-principles kinetic simulations to a complex astrophysical object such as an AGN corona requires careful consideration. In this work, we have self-consistently determined the physical conditions at the localized shock front from first principles. The estimation presented here should be regarded as an order-of-magnitude assessment based on the microphysics established in the current paper. Nonetheless, it offers valuable insights into how the local shock acceleration process can contribute to the global energetics of the source and bridge the gap between microscopic plasma physics and macroscopic high-energy phenomena observed by IceCube.

5.2. On electron acceleration

Here we briefly comment on the simulations marked with a star symbol in Figure 8, in which the nonthermal electron power-law tail does not extend to progressively higher energies with time, as noted in Section 4.3. In the trans-relativistic shock regime explored in this work, strongly amplified magnetic fields produced by ion-streaming instabilities can make the shock intermittently superluminal. Electrons with gyroradii smaller than the saturated wavelength of the ion-streaming instabilities can be affected by the amplification (T. Jikei et al. 2025). In such cases, electrons are unable to propagate far upstream of the shock and repeatedly cross it, leading to a suppression of DSA. Then, the maximum energy will be set by pre-acceleration mechanisms operating close to the shock front, such as SDA rather than growing with time.

Our results are consistent with previous findings for high-shock-velocity cases (S. Gupta et al. 2024b) and for shocks embedded in strongly amplified, locally superluminal magnetic fields (V. Zeković et al. 2025; T. Jikei et al. 2025). In these regimes, pre-acceleration processes operating near the shock can still generate non-thermal electron power-law tails extending up to $\gamma_e \sim 10^2$. However, in the absence of sustained DSA, the maximum electron energy saturates and does not increase secularly with time, being limited by the characteristic scale of the pre-acceleration mechanisms or by the typical wavelength of the amplified magnetic fluctuations. We further note that this effect is not expected to have a strong impact on black hole coronae, as such suppression occurs only for shock parameters associated with extremely strong magnetic-field amplification ($\delta B/B_0 \gg 1$), including low ion temperatures (i.e., low M_s or T_i/T_e ; see also Figure 8) or very large Alfvénic Mach numbers ($M_A \gg 1$). These conditions that are unlikely to be realized in BH coronal environments.

Finally, the generally low electron acceleration efficiency at large T_i/T_e can be attributed to the injection conditions for electrons at quasi-parallel shocks. Previous studies have pointed out that the electron thermal speed sets the threshold for injection into acceleration processes (S. Gupta et al. 2025), and that initially cold electrons must be pre-heated by another mechanism before they can be injected (S. Gupta et al. 2024a). Therefore, we naturally expect that a higher T_e (i.e., lower T_i/T_e) would be more favorable for electron acceleration. It remains unclear whether a much longer simulation would show that pre-heating of background electrons in the upstream region could increase their temperature sufficiently near the shock for efficient acceleration. A detailed investigation of electron suppression by strong amplified field, pre-heating, and acceleration signatures in these regimes is beyond the scope of the present paper and will be addressed in our upcoming work.

6. CONCLUSION

Recent IceCube observations of TeV neutrinos from the Seyfert galaxy NGC 1068 suggest efficient proton acceleration within the BH coronae. To investigate the viability of DSA in this context, we systematic performed a series of 1D3V PIC simulations of quasi-parallel shocks. Our parameter survey covers the specific regimes motivated by BH coronae, including trans-relativistic shock velocities and varying ion-to-electron temperature ratios (T_i/T_e), while systematically varying the sonic (M_s) and Alfvénic Mach numbers (M_A).

Our primary findings are as follows:

1. **Strong Shocks and Turbulence Generation:** Under coronal conditions, strong shocks can form and drive intense upstream magnetic fluctuations mediated by back-streaming ions, providing the scattering environment necessary for DSA. The turbulence is predominantly driven by the NRI across most of the parameter space, with RI modes becoming significant only at the lowest Alfvénic Mach numbers.
2. **Proton Acceleration Dynamics:** We identify clear non-thermal ion power-law tails where the maximum energy increases linearly with time after the establishment of a quasi-steady shock structure. The proton acceleration rate scales with the square of the shock velocity, $(v_{\text{sh}}/c)^2$, and linearly with the magnetic field strength (via the proton gyrofrequency, Ω_{ci}). This scaling is consistent with the standard Bohm-type diffusion in DSA theory.
3. **Universal Acceleration Rate:** Based on this scaling, we introduce a normalized acceleration rate, $\mathcal{C}^{-1} \equiv d(\gamma\beta_{\text{sh}}^{-2})/d(t\Omega_{\text{ci}})$. We find a characteristic universal value of $\mathcal{C}^{-1} \simeq 0.1$, which varies by less than a factor of 2 across our full survey (Section 4.2). This rate exhibits almost no dependence on M_s or v_{sh} and only a weak dependence on T_i/T_e . Modest reductions occur only at very low M_A (weaker self-generated turbulence) or very high M_A (disruption by intermittent magnetic structures).
4. **Ion Energy Partition:** The downstream non-thermal ion energy fraction is maintained at $\sim 10\%$ of the total shock kinetic energy across essentially all explored parameters (Section 4.3). Remarkably, efficient proton acceleration persists even at sonic Mach numbers as low as $M_s \simeq 2$, a regime previously considered unfavorable for strong non-thermal particle production.
5. **Electron Acceleration Efficiency:** We find that electron acceleration is energetically subdominant in our survey. The non-thermal electron fraction is $\lesssim 1\%$, and is typically $\sim 10^{-3}$ for coronal-like T_i/T_e . This fraction decreases with increasing T_i/T_e . For several trans-relativistic runs with extreme magnetic-field amplification, the electron cutoff energy saturates, suggesting that sustained electron DSA is inhibited when the amplified fields intermittently make the shock effectively superluminal for electrons (Section 5.2).

These kinetic results provide strong physical support for the scenario where IceCube neutrinos originate from DSA-accelerated protons. Applying our derived normalized rate ($\mathcal{C}^{-1} \simeq 0.1$) to the specific conditions of NGC 1068, we demonstrate that protons can be accelerated to ~ 100 TeV on timescales shorter than the relevant cooling and dynamical limits (Section 5.1). Furthermore, the non-thermal proton power required to explain the observed neutrino luminosity represents only a few percent of the estimated shock power—well within the 10% efficiency limit found in our simulations. Thus, shocks in SMBH coronae can naturally satisfy both the spectral and energetic requirements for neutrino production, while accompanying gamma rays are attenuated by the intense coronal radiation field.

ACKNOWLEDGMENTS

This work was partly achieved through the use of SQUID at D3 Center, The University of Osaka. Numerical computations were also carried out on HPE Cray XD2000 at the Center for Computational Astrophysics, National Astronomical Observatory of Japan and on supercomputer "Flow" at Informatioin Technology Center, Nagoya University. This research was supported by JSPS KAKENHI Grants No. JP24H00204. YI is supported by NAOJ ALMA Scientific Research Grant Number 2021-17A; JSPS KAKENHI Grant Number JP18H05458, JP19K14772, and JP22K18277; and World Premier International Research Center Initiative (WPI), MEXT, Japan.

APPENDIX

A. COMPLETE ION AND ELECTRON DOWNSTREAM SPECTRA

In this appendix, we present the downstream ion and electron spectra for the full suite of simulations, following the format of the reference run shown in Figure 3(a). Figure 10 displays cases with fixed $M_A = 26$ and $v_{\text{pt}}/c = 0.25$, but varying sonic Mach numbers and temperature ratios; here, we focus on the low sonic Mach number regime ($M_s \leq 8$).

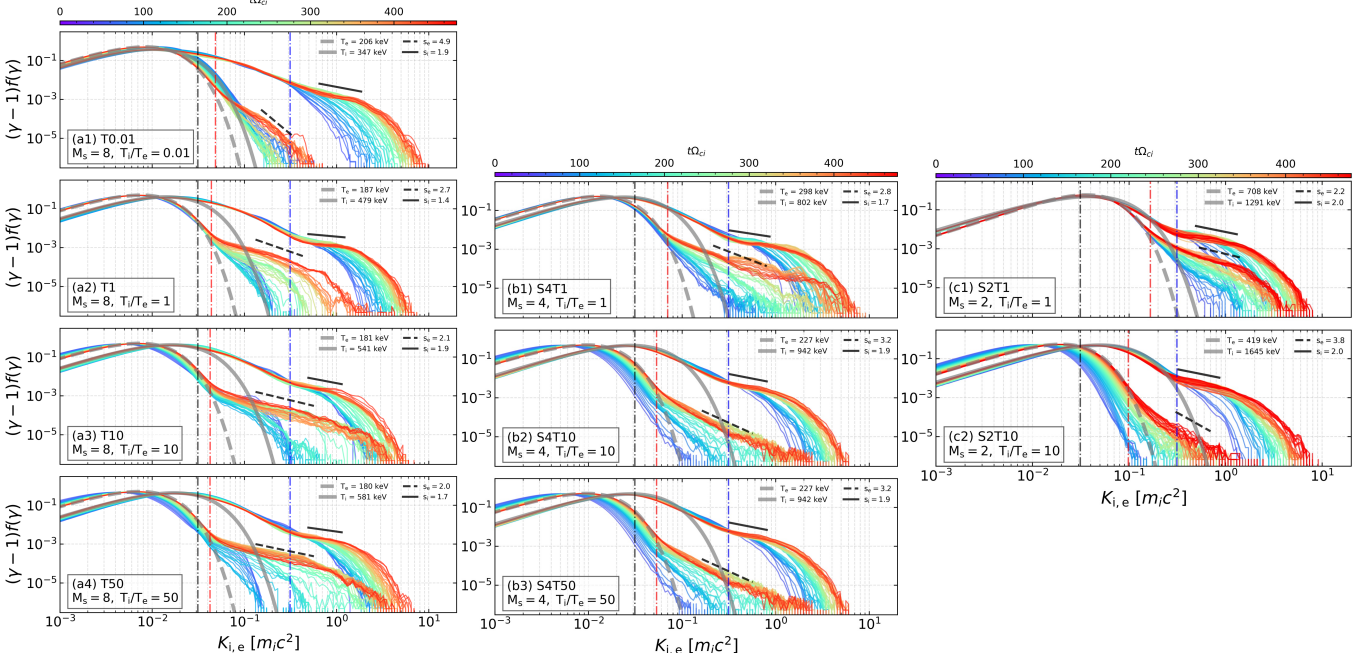


Figure 10. Downstream spectra of ions and electrons for all simulations with fixed $M_A = 26$ and $v_{pt}/c = 0.25$. Left panels (a1)–(a4) show cases with $M_s = 8$ while varying T_i/T_e from 0.01 to 50 [runs T0.01, T1, T10 (reference run), and T50]. Middle panels (b1)–(b3) correspond to simulations with fixed $M_s = 4$ and $T_i/T_e = 1$ –50 (runs S4T1, S4T10, and S4T50). Right panels (c1) and (c2) display simulations with $M_s = 2$ and $T_i/T_e = 1$ and 10 (runs S2T1 and S2T10)

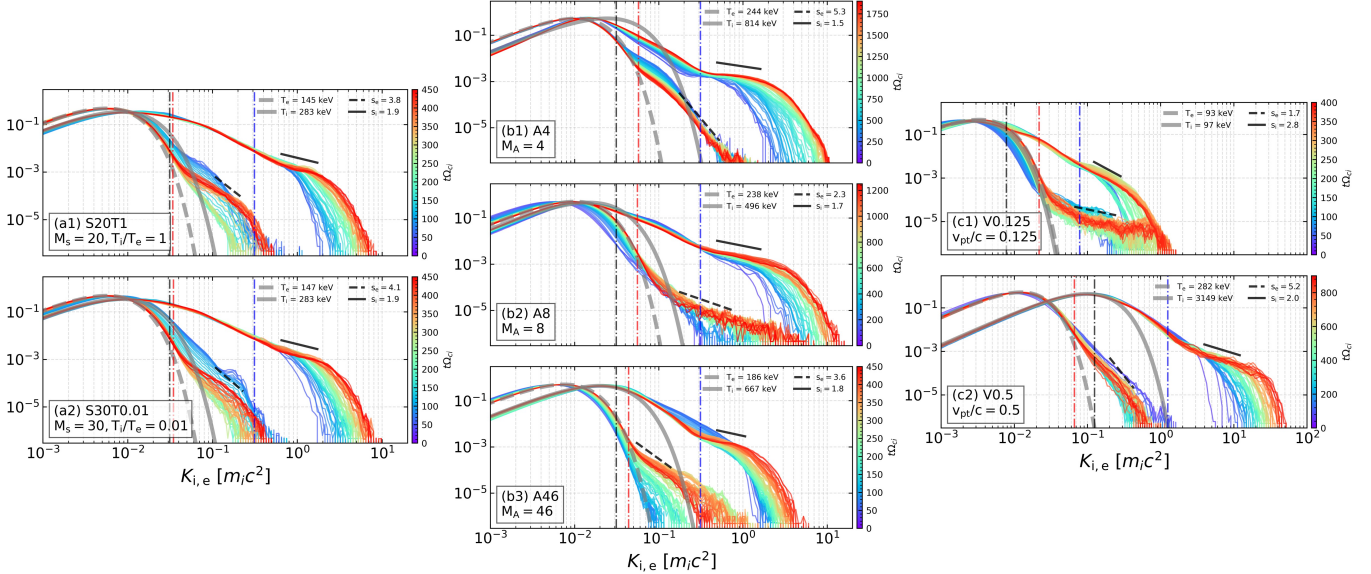


Figure 11. Downstream spectra of ions and electrons for simulations with high M_s , varying M_A , and varying v_{pt} . Left panels, (a1) and (a2), show high sonic Mach number cases ($M_s = 20$ and 30) with fixed $M_A = 26$ and $v_{pt}/c = 0.25$, similar to Figure 10. The middle and right panels share fixed $M_s = 8$ and $T_i/T_e = 10$. Middle panels (b1)–(b3) correspond to simulations with fixed $v_{pt}/c = 0.25$ and varying M_A (runs A4, A8, and A46). Right panels (c1) and (c2) display varying v_{pt}/c (0.125 and 0.5) with fixed M_A (runs V0.125 and V0.5)

High sonic Mach number cases (representing the cold inflow scenario described in Section 2) are presented in the left panels of Figure 11. Additionally, the middle and right panels of Figure 11 display spectra for simulations with varying M_A (at fixed $v_{pt}/c = 0.25$) and varying v_{pt}/c (at fixed $M_A = 26$), respectively.

REFERENCES

Abbasi, R., Ackermann, M., Adams, J., et al. 2022, *Science*, 378, 538, doi: [10.1126/science.abg3395](https://doi.org/10.1126/science.abg3395)

Abbasi, R., Ackermann, M., Adams, J., et al. 2025, Evidence for a Spectral Break or Curvature in the Spectrum of Astrophysical Neutrinos from $5\text{TeV} - 10\text{PeV}$, arXiv, doi: [10.48550/arXiv.2507.22233](https://doi.org/10.48550/arXiv.2507.22233)

Bell, A. R. 2004, *Monthly Notices of the Royal Astronomical Society*, 353, 550, doi: [10.1111/j.1365-2966.2004.08097.x](https://doi.org/10.1111/j.1365-2966.2004.08097.x)

Blandford, R., & Eichler, D. 1987, *Physics Reports*, 154, 1, doi: [10.1016/0370-1573\(87\)90134-7](https://doi.org/10.1016/0370-1573(87)90134-7)

Caprioli, D., & Spitkovsky, A. 2014a, *The Astrophysical Journal*, 783, 91, doi: [10.1088/0004-637X/783/2/91](https://doi.org/10.1088/0004-637X/783/2/91)

Caprioli, D., & Spitkovsky, A. 2014b, *The Astrophysical Journal*, 794, 46, doi: [10.1088/0004-637X/794/1/46](https://doi.org/10.1088/0004-637X/794/1/46)

Das, A., Zhang, B. T., & Murase, K. 2024, *The Astrophysical Journal*, 972, 44, doi: [10.3847/1538-4357/ad5a04](https://doi.org/10.3847/1538-4357/ad5a04)

Derouillat, J., Beck, A., Pérez, F., et al. 2018, *Computer Physics Communications*, 222, 351, doi: [10.1016/j.cpc.2017.09.024](https://doi.org/10.1016/j.cpc.2017.09.024)

Drury, L. O. 1983, *Reports on Progress in Physics*, 46, 973, doi: [10.1088/0034-4885/46/8/002](https://doi.org/10.1088/0034-4885/46/8/002)

Drury, L. O. 2012, *Astroparticle Physics*, 39-40, 52, doi: [10.1016/j.astropartphys.2012.02.006](https://doi.org/10.1016/j.astropartphys.2012.02.006)

Fabian, A. C., Lohfink, A., Kara, E., et al. 2015, *Monthly Notices of the Royal Astronomical Society*, 451, 4375, doi: [10.1093/mnras/stv1218](https://doi.org/10.1093/mnras/stv1218)

Fiorillo, D. F. G., Comisso, L., Peretti, E., Petropoulou, M., & Sironi, L. 2024a, *The Astrophysical Journal*, 974, 75, doi: [10.3847/1538-4357/ad7021](https://doi.org/10.3847/1538-4357/ad7021)

Fiorillo, D. F. G., Petropoulou, M., Comisso, L., Peretti, E., & Sironi, L. 2024b, *The Astrophysical Journal Letters*, 961, L14, doi: [10.3847/2041-8213/ad192b](https://doi.org/10.3847/2041-8213/ad192b)

Gupta, S., Caprioli, D., & Spitkovsky, A. 2024a, *The Astrophysical Journal*, 968, 17, doi: [10.3847/1538-4357/ad3e75](https://doi.org/10.3847/1538-4357/ad3e75)

Gupta, S., Caprioli, D., & Spitkovsky, A. 2024b, *The Astrophysical Journal*, 976, 10, doi: [10.3847/1538-4357/ad7c4c](https://doi.org/10.3847/1538-4357/ad7c4c)

Gupta, S., Caprioli, D., & Spitkovsky, A. 2025, Speed-dependent Threshold for Electron Injection into Diffusive Shock Acceleration, arXiv, doi: [10.48550/arXiv.2506.09134](https://doi.org/10.48550/arXiv.2506.09134)

Ha, J.-H., Ryu, D., Kang, H., & Marle, A. J. V. 2018, *The Astrophysical Journal*, 864, 105, doi: [10.3847/1538-4357/aad634](https://doi.org/10.3847/1538-4357/aad634)

Haggerty, C. C., & Caprioli, D. 2019, *The Astrophysical Journal*, 887, 165, doi: [10.3847/1538-4357/ab58c8](https://doi.org/10.3847/1538-4357/ab58c8)

Hankla, A., Philippov, A., Mbarek, R., et al. 2025, arXiv e-prints, arXiv:2512.01662, doi: [10.48550/arXiv.2512.01662](https://doi.org/10.48550/arXiv.2512.01662)

Hillas, A. M. 1984, *Annual Review of Astronomy and Astrophysics*, 22, 425, doi: [10.1146/annurev.aa.22.090184.002233](https://doi.org/10.1146/annurev.aa.22.090184.002233)

Inoue, S., Cerruti, M., Murase, K., & Liu, R.-Y. 2022, arXiv e-prints, arXiv:2207.02097, doi: [10.48550/arXiv.2207.02097](https://doi.org/10.48550/arXiv.2207.02097)

Inoue, Y., & Doi, A. 2018, *The Astrophysical Journal*, 869, 114, doi: [10.3847/1538-4357/aaeb95](https://doi.org/10.3847/1538-4357/aaeb95)

Inoue, Y., Khangulyan, D., & Doi, A. 2020, *ApJL*, 891, L33, doi: [10.3847/2041-8213/ab7661](https://doi.org/10.3847/2041-8213/ab7661)

Inoue, Y., Khangulyan, D., Inoue, S., & Doi, A. 2019, *The Astrophysical Journal*, 880, 40, doi: [10.3847/1538-4357/ab2715](https://doi.org/10.3847/1538-4357/ab2715)

Inoue, Y., Takasao, S., & Khangulyan, D. 2024, Upper Limit on the Coronal Cosmic Ray Energy Budget in Seyfert Galaxies, arXiv, doi: [10.48550/arXiv.2401.07580](https://doi.org/10.48550/arXiv.2401.07580)

Jana, A., Ricci, C., Venselaar, S. M., et al. 2025, *A&A*, 699, A62, doi: [10.1051/0004-6361/202554491](https://doi.org/10.1051/0004-6361/202554491)

Jikei, T., Groselj, D., & Sironi, L. 2025, Magnetic Field Amplification and Particle Acceleration in Weakly Magnetized Trans-relativistic Electron-ion Shocks, arXiv, doi: [10.48550/arXiv.2512.03169](https://doi.org/10.48550/arXiv.2512.03169)

Kang, H., Ryu, D., & Ha, J.-H. 2019, *The Astrophysical Journal*, 876, 79, doi: [10.3847/1538-4357/ab16d1](https://doi.org/10.3847/1538-4357/ab16d1)

Karavola, D., Petropoulou, M., Fiorillo, D. F. G., Comisso, L., & Sironi, L. 2025, Neutrino and pair creation in reconnection-powered coronae of accreting black holes, arXiv, doi: [10.48550/arXiv.2410.12638](https://doi.org/10.48550/arXiv.2410.12638)

Kato, T. N. 2015, *The Astrophysical Journal*, 802, 115, doi: [10.1088/0004-637X/802/2/115](https://doi.org/10.1088/0004-637X/802/2/115)

Kawabata, R., & Mineshige, S. 2010, *PASJ*, 62, 621, doi: [10.1093/pasj/62.3.621](https://doi.org/10.1093/pasj/62.3.621)

Kelner, S. R., & Aharonian, F. A. 2008, *Physical Review D*, 78, 034013, doi: [10.1103/PhysRevD.78.034013](https://doi.org/10.1103/PhysRevD.78.034013)

Kelner, S. R., Aharonian, F. A., & Bugayov, V. V. 2006, *Physical Review D*, 74, 034018, doi: [10.1103/PhysRevD.74.034018](https://doi.org/10.1103/PhysRevD.74.034018)

Kheirandish, A., Murase, K., & Kimura, S. S. 2021, *The Astrophysical Journal*, 922, 45, doi: [10.3847/1538-4357/ac1c77](https://doi.org/10.3847/1538-4357/ac1c77)

Laha, S., Ricci, C., Mather, J. C., et al. 2025, *Frontiers in Astronomy and Space Sciences*, 11, 1530392, doi: [10.3389/fspas.2024.1530392](https://doi.org/10.3389/fspas.2024.1530392)

Lemoine, M., & Rieger, F. 2025, *Astronomy & Astrophysics*, 697, A124, doi: [10.1051/0004-6361/202453296](https://doi.org/10.1051/0004-6361/202453296)

Marcowith, A., Van Marle, A. J., & Plotnikov, I. 2021, Physics of Plasmas, 28, 080601, doi: [10.1063/5.0013662](https://doi.org/10.1063/5.0013662)

Mbarek, R., Philippov, A., Chernoglazov, A., Levinson, A., & Mushotzky, R. 2024, Physical Review D, 109, L101306, doi: [10.1103/PhysRevD.109.L101306](https://doi.org/10.1103/PhysRevD.109.L101306)

Michiyama, T., Inoue, Y., & Doi, A. 2023, PASJ, 75, 874, doi: [10.1093/pasj/pasad044](https://doi.org/10.1093/pasj/pasad044)

Michiyama, T., Inoue, Y., Doi, A., et al. 2024, ApJ, 965, 68, doi: [10.3847/1538-4357/ad2fae](https://doi.org/10.3847/1538-4357/ad2fae)

Murase, K. 2022, The Astrophysical Journal Letters, 941, L17, doi: [10.3847/2041-8213/aca53c](https://doi.org/10.3847/2041-8213/aca53c)

Murase, K., Kimura, S. S., & Mészáros, P. 2020, Physical Review Letters, 125, 011101, doi: [10.1103/PhysRevLett.125.011101](https://doi.org/10.1103/PhysRevLett.125.011101)

Mutie, I. M., Del Palacio, S., Beswick, R. J., et al. 2025, Monthly Notices of the Royal Astronomical Society, 539, 808, doi: [10.1093/mnras/staf524](https://doi.org/10.1093/mnras/staf524)

Müller, A. L., Naddaf, M.-H., Zajaček, M., et al. 2022, The Astrophysical Journal, 931, 39, doi: [10.3847/1538-4357/ac660a](https://doi.org/10.3847/1538-4357/ac660a)

Müller, A. L., & Romero, G. E. 2020, Astronomy & Astrophysics, 636, A92, doi: [10.1051/0004-6361/202037639](https://doi.org/10.1051/0004-6361/202037639)

Oka, M., Makishima, K., & Terasawa, T. 2025, The Astrophysical Journal, 979, 161, doi: [10.3847/1538-4357/ad9916](https://doi.org/10.3847/1538-4357/ad9916)

Padovani, P., Resconi, E., Ajello, M., et al. 2024, High-energy neutrinos from the vicinity of the supermassive black hole in NGC 1068, arXiv. [http://arxiv.org/abs/2405.20146](https://arxiv.org/abs/2405.20146)

Palacio, S. d., Yang, C., Aalto, S., et al. 2025, Astronomy & Astrophysics, 701, A41, doi: [10.1051/0004-6361/202554936](https://doi.org/10.1051/0004-6361/202554936)

Park, J., Caprioli, D., & Spitkovsky, A. 2015, Physical Review Letters, 114, 085003, doi: [10.1103/PhysRevLett.114.085003](https://doi.org/10.1103/PhysRevLett.114.085003)

Park, J., Workman, J. C., Blackman, E. G., Ren, C., & Siller, R. 2012, Physics of Plasmas, 19, 062904, doi: [10.1063/1.4729913](https://doi.org/10.1063/1.4729913)

Shablovinskaya, E., Ricci, C., Chang, C.-S., et al. 2024, A&A, 690, A232, doi: [10.1051/0004-6361/202450133](https://doi.org/10.1051/0004-6361/202450133)

Shakura, N. I., & Sunyaev, R. A. 1973, Astronomy and Astrophysics, 24, 337. <https://ui.adsabs.harvard.edu/abs/1973A&A....24..337S>

Shalaby, M. 2024, The Astrophysical Journal Letters, 977, L43, doi: [10.3847/2041-8213/ad99d8](https://doi.org/10.3847/2041-8213/ad99d8)

Skilling, J. 1971, The Astrophysical Journal, 170, 265, doi: [10.1086/151210](https://doi.org/10.1086/151210)

Sotomayor, P., & Romero, G. E. 2022, Astronomy & Astrophysics, 664, A178, doi: [10.1051/0004-6361/202243682](https://doi.org/10.1051/0004-6361/202243682)

van Marle, A. J. 2020, Monthly Notices of the Royal Astronomical Society, 496, 3198, doi: [10.1093/mnras/staa1771](https://doi.org/10.1093/mnras/staa1771)

Vink, J., & Yamazaki, R. 2014, ApJ, 780, 125, doi: [10.1088/0004-637X/780/2/125](https://doi.org/10.1088/0004-637X/780/2/125)

Yasuda, K., Sakai, N., Inoue, Y., & Kusenko, A. 2025, Physical Review Letters, 134, 151005, doi: [10.1103/PhysRevLett.134.151005](https://doi.org/10.1103/PhysRevLett.134.151005)

Yuan, F., & Narayan, R. 2014, Annual Review of Astronomy and Astrophysics, 52, 529, doi: [10.1146/annurev-astro-082812-141003](https://doi.org/10.1146/annurev-astro-082812-141003)

Zeković, V., Spitkovsky, A., & Hemler, Z. 2025, The Astrophysical Journal, 988, 40, doi: [10.3847/1538-4357/ade05f](https://doi.org/10.3847/1538-4357/ade05f)